

Momentum and energy injection by a wind-blown bubble into an inhomogeneous interstellar medium

J. M. Pittard^{*}

School of Physics and Astronomy, University of Leeds, Woodhouse Lane, Leeds LS2 9JT, UK

Accepted 2022 July 07. Received 2022 July 02; in original form 2022 January 17

ABSTRACT

We investigate the effect of mass-loading from embedded clouds on the evolution of wind-blown bubbles. We use 1D hydrodynamical calculations and assume that the clouds are numerous enough that they can be treated in the continuous limit, and that rapid mixing occurs so that the injected mass quickly merges with the global flow. The destruction of embedded clouds adds mass into the bubble, increasing its density. Mass-loading increases the temperature of the unshocked stellar wind due to the frictional drag, and reduces the temperature of the hot shocked gas as the available thermal energy is shared between more particles. Mass-loading may increase or decrease the volume-averaged bubble pressure. Mass-loaded bubbles are smaller, have less retained energy and lower radial momentum, but in all cases examined are still able to do significant PdV work on the swept-up gas. In this latter respect, the bubbles more closely resemble energy-conserving bubbles than the momentum-conserving-like behaviour of “quenched” bubbles.

Key words: ISM: bubbles – ISM: kinematics and dynamics – stars: massive – stars: winds, outflows – stars: early-type – galaxies: ISM

1 INTRODUCTION

Massive stars are key agents affecting star formation in galaxies. On local scales they rapidly destroy star-forming molecular clouds, through their intense radiation, powerful winds and supernova explosions. Early (pre-supernova) feedback seems to be important, since it is needed to explain the anti-correlation of giant molecular clouds (GMCs) and ionized regions on 100 pc scales and less (e.g. [Chevance et al. 2022](#)). On larger galactic scales, supernova feedback seems to be the dominant of the three mechanisms, determining the amplitude of turbulent gas motions that limit and control star formation (e.g. [Shetty & Ostriker 2012](#)).

The importance of stellar wind feedback is still uncertain. It is clear that the ability of a wind-blown bubble (WBB) to do PdV work on surrounding gas depends on the interior of the bubble remaining hot. Recent work has demonstrated that turbulent mixing at the interface between the hot interior gas and colder exterior gas can set the cooling losses for the entire bubble. [El-Badry et al. \(2019\)](#) used a 1D simulation with an effective model for interface mixing and turbulence, and found a reduction in the radial momentum of a factor of 2. In the extreme case that the interface becomes fractal-like, perhaps helped by perturbations due to the inhomogeneity of the surrounding gas, radiative losses might become so strong that the bubble displays momentum-conserving-like behaviour ([Lancaster et al. 2021a,b](#)). Work to understand the effect of embedded clouds on surrounding hotter gas includes analytical studies (e.g. [Cowie & McKee 1977](#); [Hartquist et al. 1986](#); [Fielding & Bryan 2022](#)), and simulations (e.g. [Cowie, McKee & Ostriker 1981](#); [Korolev et al.](#)

[2015](#); [Kim, Ostriker & Raileanu 2017](#); [Slavin et al. 2017](#); [Zhang & Chevalier 2019](#); [Farber & Gronke 2022](#)).

Another issue is that numerical simulations of wind-blown bubbles have not always had the necessary resolution for the bubble to properly inflate. Under-resolved bubbles do not produce the correct amount of PdV work on the surrounding gas, and so have less impact on their surroundings than they should¹. [Pittard, Wareing & Kupilas \(2021\)](#) determined the resolution requirements for the wind injection radius to correctly inflate the bubble.

In this work we reexamine the effect of mass-loading from embedded clouds/clumps on the evolution of wind-blown bubbles. We note three issues that arise in 3D simulations which directly model cloud interactions with a larger-scale flow. First, such simulations almost always suffer from insufficient numerical resolution, which means that the clouds will accelerate and mix up to 5× faster than they should ([Pittard & Parkin 2016](#)). A second issue concerns cooling at hot-cold interfaces. [Parkin & Pittard \(2010\)](#) showed that due to numerical conduction, the amount of cooling is dependent on the numerical resolution employed². A final issue is that when hot-cold interfaces advect across grid cells, such as when a cold cloud surrounded by hot gas moves across the grid, intermediate temperature grid cells are created, which then suffer from anomalously high cooling.

To avoid these issues, we do not directly model the clouds in this

¹ This issue is akin to the “over-cooling” problem that early simulations of supernova feedback suffered from (e.g. [Katz 1992](#)).

² In contrast, simulations of turbulent mixing layers by [Fielding et al. \(2020\)](#) showed that the numerical resolution did not have a large effect on the amount of cooling. A definitive answer will require a correct treatment of conduction and the scale dependence of the fractal nature of mixing layers, which has not yet been fully carried out in the literature.

^{*} E-mail: j.m.pittard@leeds.ac.uk (JMP)

work, but instead assume that they are numerous and continuously distributed in the surrounding medium. We then assume that the clouds that are overrun by the bubble are destroyed within the bubble interior and inject mass into the bubble at a global rate that is proportional to the mass-loss rate of the star³. We assume that the flow can be treated as a single fluid, which requires that the material liberated from the clouds rapidly merges with the global flow and attains the same density, velocity and temperature.

With these assumptions, cloud destruction affects cooling in the bubble only through the change in density and temperature associated with the addition of (fully-mixed) mass into it, and not through enhanced cooling at (potentially unresolved) interfaces. By minimising cooling at hot-cold interfaces in this work, we take an opposing position to direct simulations of WBBs in an inhomogeneous medium (which may well overestimate the cooling). Our work follows the same approach taken by Pittard (2019), who investigated the evolution of mass-loaded supernova remnants (SNRs). In Section 2 we note the specific details of our calculations. In Section 3 we present our results. In Section 4 we discuss the validity of our assumptions and compare our findings to previous theoretical and observational work. In Section 5 we summarize and conclude our work.

2 THE CALCULATIONS

We use a modified version of the VH-1 code⁴ to perform the calculations. This code solves the standard inviscid equations of 1D spherical hydrodynamics in conservative Lagrangian form, for the conservation of mass, momentum and energy, respectively:

$$\frac{\partial \tau}{\partial t} - \frac{\partial(r^2 u)}{\partial m} = \dot{\tau}, \quad (1)$$

$$\frac{\partial u}{\partial t} + r^2 \frac{\partial P}{\partial m} = 0, \quad (2)$$

$$\frac{\partial E}{\partial t} + \frac{\partial(r^2 u P)}{\partial m} = \dot{E}, \quad (3)$$

where τ is the specific volume ($\rho = 1/\tau$ is the fluid mass density), u is the velocity, and P is the pressure. $E = \rho u^2/2 + P/(\gamma - 1)$ is the total energy per unit volume, where $\gamma = 5/3$ is the ratio of specific heats. The mass coordinate m is defined by $dm = \rho r^2 dr$, where r is the radial coordinate.

Piecewise parabolic spatial reconstruction is applied to the fluid variables to obtain values at each cell interface. These are input into the iterative, approximate two-shock Riemann solver of Colella & Woodward (1984). This outputs the time-averaged fluxes at each interface to update the fluid variables. Finally, the updated quantities are remapped to the original grid at the end of every step. This approach is known as PPMLR: Piecewise Parabolic Method with Lagrangian Remap.

Two source terms are added to the hydrodynamic equations which are treated via operator splitting. Firstly, the rate of change of the internal energy per unit volume due to heating and cooling is:

$$\dot{E} = (\rho/m_{\text{H}})\Gamma - (\rho/m_{\text{H}})^2\Lambda(T), \quad (4)$$

where the temperature-independent heating coefficient $\Gamma = 2 \times$

$10^{-26} \text{ erg s}^{-1}$. The cooling curve, $\Lambda(T)$, is calculated assuming collisional ionization equilibrium and is constructed from 3 separate parts (for further details see Wareing, Pittard & Falle 2017a,b; Kupilas et al. 2021; Pittard, Kupilas & Wareing 2022). We assume solar abundances with mass fractions $X_{\text{H}} = 0.7381$, $X_{\text{He}} = 0.2485$, and $X_{\text{Z}} = 0.0134$ (cf. Grevesse et al. 2010). We also use a temperature-dependent average particle mass, which is determined from a look-up table of values of P/ρ (Sutherland 2010).

The second source term is the rate of change of the specific volume due to cloud destruction, $\dot{\tau} = -\dot{\rho}/\rho^2$. We assume that the clumps inject mass at a global rate inside the bubble of $\dot{M}_{\text{cl}} = f_{\text{ML}} \dot{M}_{\text{w}}$, where \dot{M}_{w} is the mass-loss rate of the star and f_{ML} is the mass-loading factor which sets the relative strength of the mass-loading. We assume that the mass injection occurs uniformly within the bubble⁵, so that the rate of change of the gas density is given by

$$\dot{\rho} = f_{\text{ML}} \dot{M}_{\text{w}}/V_{\text{bub}}, \quad (5)$$

where $V_{\text{bub}} = \frac{4}{3}\pi r_{\text{FS}}^3$ is the volume of the WBB and r_{FS} is the radius of the forward shock. Mass-loading occurs inside the WBB (including in the swept-up shell) but outside the injection region of the wind. As the bubble expands and its volume increases, the mass injection rate per unit volume decreases. The injected mass is assumed to be at rest and cold before mixing with the flow so there are no momentum or energy source terms due to the mass-loading.

The mass in the clumps has no effect on the dynamics of the bubble other than to add mass to the bubble interior. The clouds have no momentum imparted to them by the bubble: they are immovable, swept-up objects that can do nothing but evaporate/mix. In reality, clouds will pick up momentum from the flow and move downstream. The exact distance that clouds travel downstream before fully mixing with the flow is not known, but will depend on such things as the cloud size and density, the density, velocity and Mach number of the flow, whether the cloud is smooth or structured, whether the cloud is impacted by a wind or a shock, and whether magnetic fields, thermal conduction and radiative cooling are important (see, e.g., Klein, McKee & Colella 1994; Nakamura et al. 2006; Scannapieco & Brüggén 2015; McCourt et al. 2015; Brüggén & Scannapieco 2016; Pittard & Parkin 2016; Pittard & Goldsmith 2016; Goldsmith & Pittard 2016, 2017; Schneider & Robertson 2017; Goldsmith & Pittard 2018; Banda-Barragán et al. 2019; Goldsmith & Pittard 2020). In addition, the presence of other clouds can affect the interaction (e.g. Poludnenko, Frank & Blackman 2002; Alúzar et al. 2012, 2014; Forbes & Lin 2019; Banda-Barragán et al. 2020, 2021). Such complications are ignored in the current work.

An additional parameter in our calculations is the ratio of mass in clumps to the mass in interclump gas in the background, which we define as ν . The interclump background density that the bubble is expanding into is ρ_{ic} . The large-scale, smoothed-out density of clumps $\rho_{\text{cl,avg}} = \nu\rho_{\text{ic}}$, though by definition the clouds have actual densities $\rho > \rho_{\text{cl,avg}}$. Larger values of ν mean that there is a larger reservoir of cloud mass that can be injected into the WBB. Small and/or low density clouds that are relatively rare would be consistent with a small value of ν and high value of f_{ML} (rapid cloud destruction, with most of the mass injection occurring close to the forward shock). Large and/or high density clouds are consistent with a large value

³ Using 3D numerical simulations, Rogers & Pittard (2013) found that the mass-loading factor of a wind surrounded by a clumpy medium was of order several hundred.

⁴ <http://wonka.physics.ncsu.edu/pub/VH-1/>

⁵ Note, however, that this assumption is subject to the presence of available clump material, and in cases where the clump mass ‘‘runs out’’, the mass injection occurs only in the part of the bubble where clumps remain - in this scenario the model mimics clouds being quickly destroyed and mass-loading occurring only near the bubble edge.

of ν (long-lived clouds, with mass injection throughout the bubble). We keep track of the cloud mass in each grid cell which declines as mass is injected into the bubble. In regions where the local clumps are completely destroyed, which can occur when there is rapid mass-loading and a finite reservoir of mass in the clumps, no further clump mass is added to the grid cells affected. In such circumstances the global rate of mass injection into the bubble can fall below $f_{\text{ML}} \dot{M}_w$. We include advected scalars to track the mass fractions of wind, injected and ambient material in each grid cell.

We assume that the star is a single O-star, and has a mass-loss rate $\dot{M}_w = 10^{-7} M_\odot \text{yr}^{-1}$, a stellar wind speed $v_w = 2000 \text{ km s}^{-1}$, and a main-sequence lifetime $t_{\text{MS}} = 5 \text{ Myr}$ (such parameters are typical of a “late”ish O-star, e.g., [Marcolino et al. 2022](#)). During this period the star injects $0.5 M_\odot$ of mass, $10^3 M_\odot \text{ km s}^{-1}$ of momentum, and $2 \times 10^{49} \text{ erg}$ of energy into its surroundings.

[Pittard et al. \(2021\)](#) examined the effects of different wind injection mechanisms and numerical resolution on the ability of a wind-blown bubble to inflate. They found that the radius of the wind injection region, r_{inj} , needed to be significantly less than

$$r_{\text{inj,max}} = \left(\frac{\dot{M}_w v_w}{4\pi P_{\text{amb}}} \right)^{1/2}, \quad (6)$$

where P_{amb} is the pressure of the ambient medium. In this work we adopt $r_{\text{inj}} = 0.01 r_{\text{inj,max}}$, which gives an accurate value for the momentum of the bubble ([Pittard et al. 2021](#)). We use 5 cells for the injection radius. All simulations use the *meo* wind injection method (see [Pittard et al. 2021](#)).

We run a number of simulations to investigate the effect of varying the values of f_{ML} and ν on the evolution of the bubble. We also explore both low and high intercloud densities. Our models are noted in Tables 1 and 2 where we also record various properties of the bubble at the end of the simulation, including its radius, r_{FS} , the swept-up intercloud mass, M_{sw} , the mass injected into the bubble from the clumps, M_{inj} , the mass of hot gas (defined as gas with $T > 2 \times 10^4 \text{ K}$), M_{hot} , the thermal energy, E_{th} , the kinetic energy, E_{kin} , and the radial momentum, p_{bub} . Of course, the results of our study may be somewhat specific to the parameter values adopted.

3 RESULTS

3.1 “Low” intercloud density

In the following calculations we adopt an interclump number density of Hydrogen nuclei $n_{\text{H,ic}} = 1 \text{ cm}^{-3}$. This gives $\rho_{\text{ic}} = 2.267 \times 10^{-24} \text{ g cm}^{-3}$, a mean molecular weight $\mu_{\text{H,ic}} = 1.07$, and $T_{\text{ic}} = 2950 \text{ K}$. The latter two values arise from assuming thermal equilibrium with the adopted cooling curve. The pressure of the intercloud gas, $P_{\text{ic}} = 5.17 \times 10^{-13} \text{ dyn cm}^{-2}$ (or $P_{\text{ic}}/k = 3750 \text{ K cm}^{-3}$). With these parameters $r_{\text{inj,max}} = 4.51 \text{ pc}$ ($P_{\text{amb}} = P_{\text{ic}}$ in our current work). The width of each grid cell is $dr = 9.028 \times 10^{-3} \text{ pc}$.

3.1.1 No mass-loading

We begin by examining the evolution of the WBB without any mass-loading (i.e. $f_{\text{ML}} = 0$). Fig. 1a-d) shows density, temperature, pressure, and adiabatic Mach number profiles at 3 bubble ages. We see the classic bubble structure which consists of freely outflowing stellar wind, a reverse shock, a region of shocked stellar wind, a contact discontinuity, a region of swept-up ambient material, and a forward shock. The shell formation time is $\approx 2100 \text{ yr}$ (cf. Eq. 4.3 in [Koo & McKee 1992](#)). The shell is initially very thin, due to the high Mach

number of the forward shock, but thickens as the bubble expansion slows down. In the following, when we refer to the “bubble”, we mean the entire entity (shocked stellar wind, swept-up material, and in the case of mass-loading also the injected mass).

At $t = 5 \text{ Myr}$, the radii of the reverse shock, contact discontinuity and forward shock are at approximately 3.7, 41.3 and 51.5 pc, respectively. The shocked stellar wind is heated to $\approx 5 \times 10^7 \text{ K}$, and its high pressure drives the expansion of the bubble. At $t = 5 \text{ Myr}$, some of the swept-up material is in a dense and cold shell near the contact discontinuity, where the gas is compressed to about 300× the ambient intercloud density, and cools to below 30 K. However, due to the low isothermal Mach number of the forward shock at this time (≈ 1.3), material which has been more recently shocked is compressed very little, and a much thicker shocked region separates the forward shock from the densest part of the shell (at $t = 5 \text{ Myr}$ the thick shell is most clearly seen in the Mach number plot in Fig. 1d).

The pressure within the bubble is almost constant at any given moment in time, but drops markedly as the bubble expands. The bubble is over-pressured by factors of approximately 20 and 4 at $t = 0.1$ and 1 Myr, respectively. The supersonic wind has a very high Mach number, but the Mach number just after the reverse shock drops to approximately 0.4, and declines further with radius, reaching its lowest value at the contact discontinuity. The cooling of the swept-up gas means that the adiabatic Mach number increases between the forward shock and the contact discontinuity.

Fig. 1e-h) shows the evolution of the radius of the WBB, its radial momentum, the pressure inside the bubble, and the retained energy. The thin solid black line in the panels shows the analytical solution for a bubble with a hot, adiabatic interior (Eqs. 21 and 22 in [Weaver et al. \(1977\)](#) for the bubble radius and pressure; and Eq. 9 in [Pittard et al. \(2021\)](#) for the bubble radial momentum). We see that the bubble behaves generally as expected, though there are some slight disagreements with the analytical theory. The differences arise because the analytical theory assumes that the ambient pressure is much smaller than the bubble pressure. However, we see in Fig. 1g) that this is not true at late times, which is when the differences between the theoretical and model results are at their greatest. The result is that the forward shock transitions from an initially strong shock to a weak shock. Fig. 1e) shows that the forward shock isothermal Mach number is 4.5 at $t = 0.2 \text{ Myr}$, 2.5 at $t = 1 \text{ Myr}$, and just 1.35 at $t = 5 \text{ Myr}$. This causes the bubble radius to be greater than expected as the swept-up shell grows in relative thickness with time. It also causes the bubble radial momentum to drop away from the analytical value at late times (Fig. 1f)⁶.

In calculating the retained energy fraction, we note that it is important to include both the mechanical energy input by the wind *and* the integrated thermal energy of the ambient gas that has been swept up (which becomes significant at late times in this model). The energy input by the wind $E_w = \dot{E}t$, where $\dot{E} = \frac{1}{2} \dot{M}_w v_w^2$ is the mechanical luminosity of the wind. The thermal energy of the swept-up

⁶ We have confirmed that the disagreement with theory and simulation in Fig. 1e-g) is due to the ambient pressure becoming significant by repeating the calculation with a lower ambient pressure. To achieve this we artificially lowered the heating rate of gas with $T < 6000 \text{ K}$ (specifically, we multiply Γ by a factor $[1 - (6000 - T)/6000]$ for temperatures $T < 6000 \text{ K}$). This led to a much reduced temperature for the ambient intercloud material ($T_{\text{ic}} = 30.4 \text{ K}$), and a comensurate drop in the ambient pressure ($P_{\text{amb}} = 2.45 \times 10^{-15} \text{ dyn cm}^{-2}$), but it does not affect the strength of cooling in the model. With this change we find that the bubble momentum perfectly tracks the analytical theory. Analytical theory for cases where the ambient pressure is significant can be found in [García-Segura & Franco \(1996\)](#).

Table 1. Physical quantities at $t = 5$ Myr in models of WBBs expanding into an inhomogeneous ambient medium of intercloud hydrogen nucleon number density $n_{\text{H,ic}} = 1 \text{ cm}^{-3}$ ($\rho_{\text{ic}} = n_{\text{H,ic}} m_{\text{H}} / X_{\text{H}} = 2.267 \times 10^{-24} \text{ g cm}^{-3}$), temperature $T_{\text{ic}} = 2950 \text{ K}$, and pressure $P_{\text{ic}} = 5.17 \times 10^{-13} \text{ dyn cm}^{-2}$ ($P_{\text{ic}}/k = 3750 \text{ K cm}^{-3}$). The ratio of initial cloud mass to intercloud mass is ν . The injection of cloud gas into the bubble occurs at a rate $\dot{M}_{\text{cl}} = f_{\text{ML}} \dot{M}_{\text{W}}$. The measured quantities are the radius of the bubble (r_{FS}), the swept-up intercloud mass (M_{sw}), the injected mass from clump destruction (M_{inj}), the mass of “hot” gas (M_{hot}), the total thermal (E_{th}) and kinetic (E_{kin}) energies, and the radial momentum (p_{bub}). M_{hot} can sometimes show significant variation on short timescales: when this occurs the quantity is recorded in italics. Values in square brackets are normalised to the standard Weaver et al. (1977) bubble assuming an adiabatic interior and a negligible external pressure. E_{th} and E_{kin} measure the energy in the entire bubble (wind, swept-up and injected mass) but are normalized by just the thermal energy of the hot gas and the kinetic energy of the swept-up shell, respectively.

Model	f_{ML}	ν	r_{FS} (pc)	$M_{\text{sw}}/10^4$ (M_{\odot})	M_{inj} (M_{\odot})	M_{hot} (M_{\odot})	$E_{\text{th}}/10^{49}$ (erg)	$E_{\text{kin}}/10^{48}$ (erg)	$p_{\text{bub}}/10^4$ ($M_{\odot} \text{ km s}^{-1}$)
fML0	0.0	-	51.5 [1.12]	1.90 [1.41]	0.0	<i>0.54</i> [1.08]	1.62 [1.79]	1.34 [0.35]	4.18 [0.58]
fML10_nu1e10	10	10^{10}	51.5 [1.12]	1.90 [1.41]	5.0	3.1 [6.2]	1.62 [1.79]	1.34 [0.35]	4.18 [0.58]
fML100_nu1e10	10^2	10^{10}	50.5 [1.10]	1.79 [1.33]	50.0	17.6 [35.2]	1.49 [1.65]	1.16 [0.30]	3.75 [0.52]
fML1000_nu1e10	10^3	10^{10}	44.0 [0.96]	1.18 [0.88]	499	20.8 [41.6]	0.83 [0.92]	0.23 [0.06]	1.08 [0.15]
fML10_nu10	10	10	51.5 [1.12]	1.90 [1.41]	5.0	3.1 [6.2]	1.62 [1.79]	1.34 [0.35]	4.18 [0.58]
fML100_nu10	10^2	10	50.5 [1.10]	1.79 [1.33]	50.0	17.3 [34.6]	1.49 [1.65]	1.16 [0.30]	3.75 [0.52]
fML1000_nu10	10^3	10	45.0 [0.98]	1.27 [0.94]	498	21.3 [42.6]	0.89 [0.98]	0.23 [0.06]	1.08 [0.15]
fML1000_nu1	10^3	1	45.4 [0.99]	1.30 [0.96]	486	21.3 [42.6]	0.91 [1.01]	0.22 [0.06]	1.09 [0.15]
fML1000_nu0.1	10^3	0.1	48.6 [1.06]	1.60 [1.19]	395	22.4 [44.8]	1.09 [1.21]	0.25 [0.06]	1.40 [0.19]
fML1000_nu0.01	10^3	0.01	51.4 [1.12]	1.89 [1.40]	140	<i>0.50</i> [1.0]	1.61 [1.78]	1.35 [0.35]	4.19 [0.58]

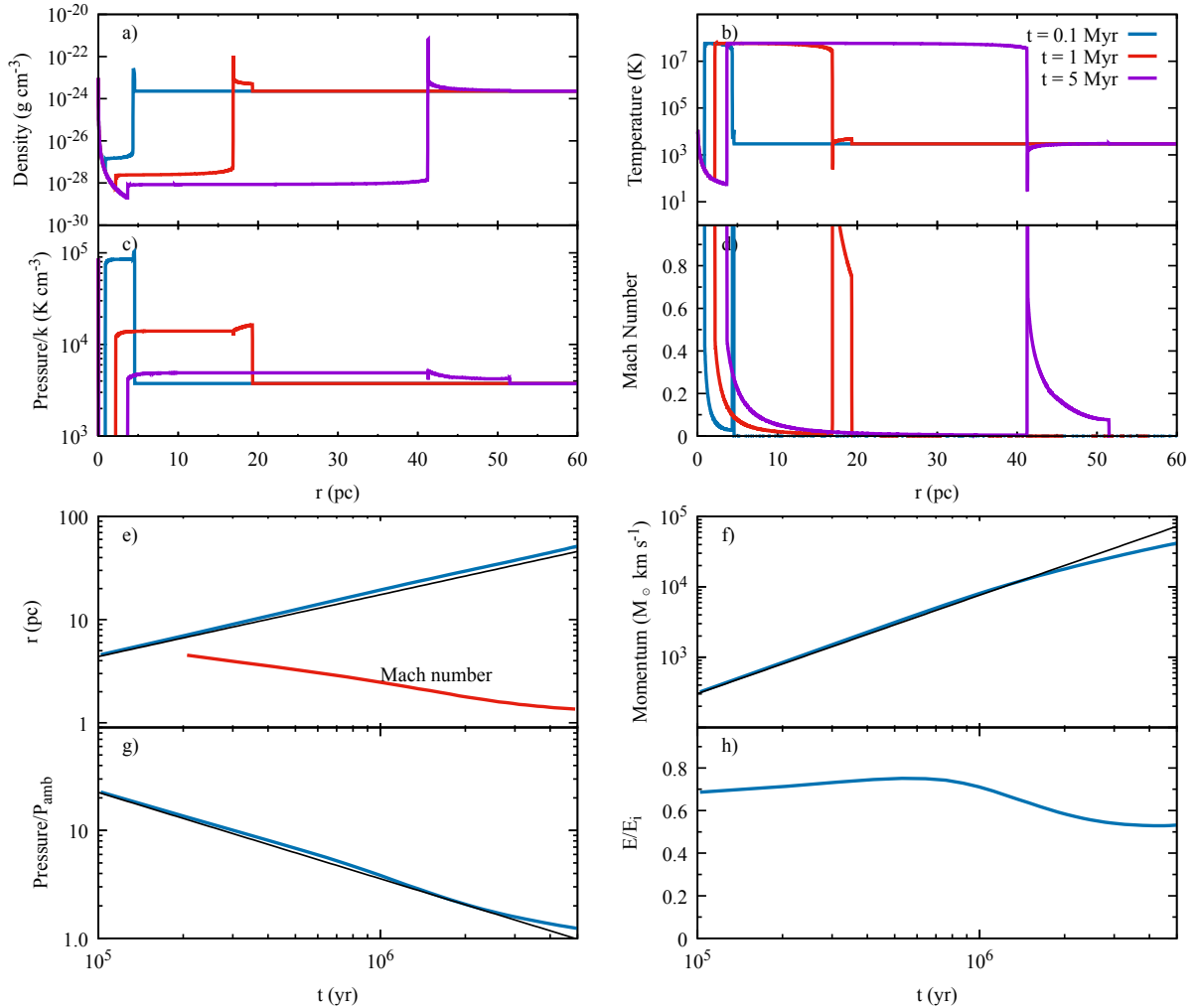


Figure 1. The evolution of a bubble with $n_{\text{H,ic}} = 1 \text{ cm}^{-3}$ ($\rho_{\text{ic}} = 2.267 \times 10^{-24} \text{ g cm}^{-3}$) and no mass-loading ($f_{\text{ML}} = 0$). Panels a-d) show profiles of the density, temperature, pressure and adiabatic Mach number at $t = 0.1, 1$ and 5 Myr. Panel e) shows the bubble radius (and the isothermal Mach number of the forward shock); f) shows the radial momentum; g) shows the volume averaged pressure; and h) shows the retained energy fraction. In panels e)-h), simulation results are shown in blue and red, and analytical results in black.

Table 2. As Table 1 but for an inhomogeneous ambient medium of intercloud hydrogen nucleon number density $n_{\text{H,ic}} = 884 \text{ cm}^{-3}$ ($\rho_{\text{ic}} = 2 \times 10^{-21} \text{ g cm}^{-3}$), temperature $T_{\text{ic}} = 21.2 \text{ K}$, and pressure $P_{\text{ic}} = 1.48 \times 10^{-12} \text{ dyn cm}^{-2}$ ($P_{\text{ic}}/k = 1.075 \times 10^4 \text{ K cm}^{-3}$).

Model	f_{ML}	ν	r_{FS} (pc)	$M_{\text{sw}}/10^5$ (M_{\odot})	M_{inj} (M_{\odot})	M_{hot} (M_{\odot})	$E_{\text{th}}/10^{48}$ (erg)	$E_{\text{kin}}/10^{48}$ (erg)	$p_{\text{bub}}/10^5$ ($M_{\odot} \text{ km s}^{-1}$)
fML0	0.0	-	11.5 [0.97]	1.88 [0.93]	0.0	0.65 [1.3]	8.31 [0.92]	3.35 [0.87]	2.51 [0.89]
fML10_nu1e10	10	10^{10}	11.4 [0.97]	1.85 [0.91]	5.0	3.7 [7.4]	8.01 [0.89]	3.23 [0.83]	2.45 [0.87]
fML100_nu1e10	10^2	10^{10}	8.51 [0.72]	0.76 [0.37]	49.9	4.36 [8.72]	1.66 [0.18]	0.64 [0.17]	0.70 [0.25]
fML1000_nu1e10	10^3	10^{10}	6.08 [0.52]	0.28 [0.14]	498	2.57 [5.14]	0.22 [0.02]	0.13 [0.03]	0.16 [0.06]

gas is $E_{\text{sw}} = 1.5 V_{\text{bub}} P_{\text{ic}}$. The total input energy is $E_i = E_w + E_{\text{sw}}$. Fig. 1h) shows that the bubble retains about 75 per cent of the input energy at $t \approx 0.5 \text{ Myr}$, but just 53 per cent at $t = 5 \text{ Myr}$ (at this time, $E_w = 2 \times 10^{49} \text{ erg}$, $E_{\text{sw}} = 1.3 \times 10^{49} \text{ erg}$, and the total energy measured in the bubble is $E = 1.75 \times 10^{49} \text{ erg}$).

In the case of an ideal adiabatic bubble expanding into a pressureless environment, $E_i = E_w$ since $E_{\text{sw}} = 0.0$. In such cases we expect the swept-up shell to have a kinetic energy of $\frac{15}{77} E_w$ (e.g. Dyson & Williams 1980). Behind a strong shock, the kinetic energy and thermal energy per unit mass are identical, so up to 19 per cent of the input energy can be radiated by the swept-up gas. This fraction is in rough agreement with the roughly 25 per cent energy loss seen at $t \approx 0.5 \text{ Myr}$, with cooling in the hot bubble and at the contact discontinuity adding the remainder. The decrease seen in the retained energy fraction between 0.5 and 5 Myr indicates that cooling of the shocked stellar wind becomes more significant as the bubble ages. Having said this, the retained energy fraction reaches a minimum near $t = 5 \text{ Myr}$ and then starts to rise slightly. This is due to the increasing significance of the thermal energy of the swept-up gas, and the fact that this gas suffers little radiative loss at late times since it is heated very little and the post-shock temperature remains close to the equilibrium temperature for gas at such densities. In any case, the retained energy fraction is always above 50 per cent, and the bubble behaviour indicates that radiative energy losses from the hot gas in the bubble interior have little consequence in this model.

In summary, we find that without mass-loading the bubble expands as expected given that the ambient pressure becomes significant at late times. The bubble does significant PdV work on the surrounding gas, boosting the radial momentum input by the wind by a factor of 40 by $t = 5 \text{ Myr}$.

3.1.2 A large reservoir of clump mass

We now examine the effect of mass-loading on a WBB. We begin by assuming that there is an effectively infinite reservoir of mass in the clumps, which never runs out. We achieve this in the simulations by setting ν to a very high value ($\nu = 10^{10}$). We explore mass-loading factors of 10^2 – 10^3 . This is motivated by estimated factors of ≈ 170 in the dusty wind-blown bubble N49 (Everett & Churchwell 2010), 40–50 in the Wolf-Rayet wind-blown-bubble RCW 58 (Smith et al. 1984) and ~ 100 in the halo of the core-halo planetary nebula NGC 6543 (Meaburn et al. 1991; Arthur, Dyson & Hartquist 1994), as well as factors of up to several hundred occurring in numerical simulations (Rogers & Pittard 2013).

In Fig. 2 we show profiles of the WBB at $t = 5 \text{ Myr}$, as a function of the strength of mass-loading. Some dramatic differences are visible in the profiles when mass-loading from embedded clumps occurs. When $f_{\text{ML}} = 10^2$ we see that the mass-loading increases the density and decreases the temperature of the shocked stellar wind gas. The latter is mainly due to sharing the thermal energy of the gas between

more particles. We see also that mass-loading of the unshocked wind increases its temperature prior to passing through the reverse shock. This is due to the frictional aspect of mass-loading. The density of this part of the flow also increases but the change is minimal in this model. We also find that the amount of mass added to a particular part of the shocked wind increases with distance from the reverse shock. This is because the oldest stellar wind material (defined as the time since being emitted from the star) is closest to the contact discontinuity. At the reverse shock the fraction of injected mass is about 4 per cent, while it increases to 99.1 per cent of the gas mass at the contact discontinuity. Mass-loading also occurs in the thick swept-up shell, but the injected mass fraction in this region remains below 2 per cent.

Fig. 2c) shows that mass-loading has reduced the pressure of the bubble at this time, although as can be seen in Fig. 2g) this is not necessarily true at earlier times for bubbles with strong mass-loading. Mass-loading also causes an increase in the Mach number of the shocked stellar wind, as expected (see Hartquist et al. 1986; Arthur, Dyson & Hartquist 1993; Arthur, Henney & Dyson 1996).

From Table 1 and Fig. 2, we see that with $f_{\text{ML}} = 10^2$ there are only minor differences in the radius, total energy and radial momentum of the bubble, indicating that the density and temperature changes within the bubble caused by the mass-loading have not resulted in significant additional radiative cooling. However, the mass of hot gas has increased from $0.54 M_{\odot}$ to $17.6 M_{\odot}$. Thus, while in this case mass-loading has not dramatically changed the dynamics of the bubble (e.g., forward shock radius, total radial momentum, etc.), it will have significantly affected its X-ray emission.

There are much more significant differences when $f_{\text{ML}} = 10^3$, the most notable being that the bubble is much smaller at early times, and the radial momentum and retained energy fraction are also much smaller than the standard bubble. To better understand this difference in behaviour, we show in Figs. 3 and 4 the early and late evolution of the $f_{\text{ML}} = 10^3$ bubble.

We see from Fig. 3b) that at $t = 0.01 \text{ Myr}$ the hottest gas has a temperature of about 10^6 K , which is far below the temperature of the bubble with no mass-loading. There is no evidence of a reverse shock at this time, and the mass-loading has an immediate and strong effect on the flow in the first grid cell outside of the wind injection region, to the extent that 97 per cent of the mass in this cell is injected from the clumps, and the velocity is slowed to 3 per cent of the wind speed. However, the wind is able to slowly push away and by $t = 0.047 \text{ Myr}$, the wind maintains 71 per cent of its initial speed and makes up 81 per cent of the mass in the first grid cell outside of the wind injection region. However, the density in this first cell still exceeds the density in the final grid cell inside the wind injection region at this time and there is still no sign of a reverse shock. Finally, by $t = 0.1 \text{ Myr}$, a (very weak) reverse shock is established at $r = 0.15 \text{ pc}$ (this is best seen in the pressure jump in Fig. 3c).

Pittard et al. (2021) showed that simulations of wind-blown bub-

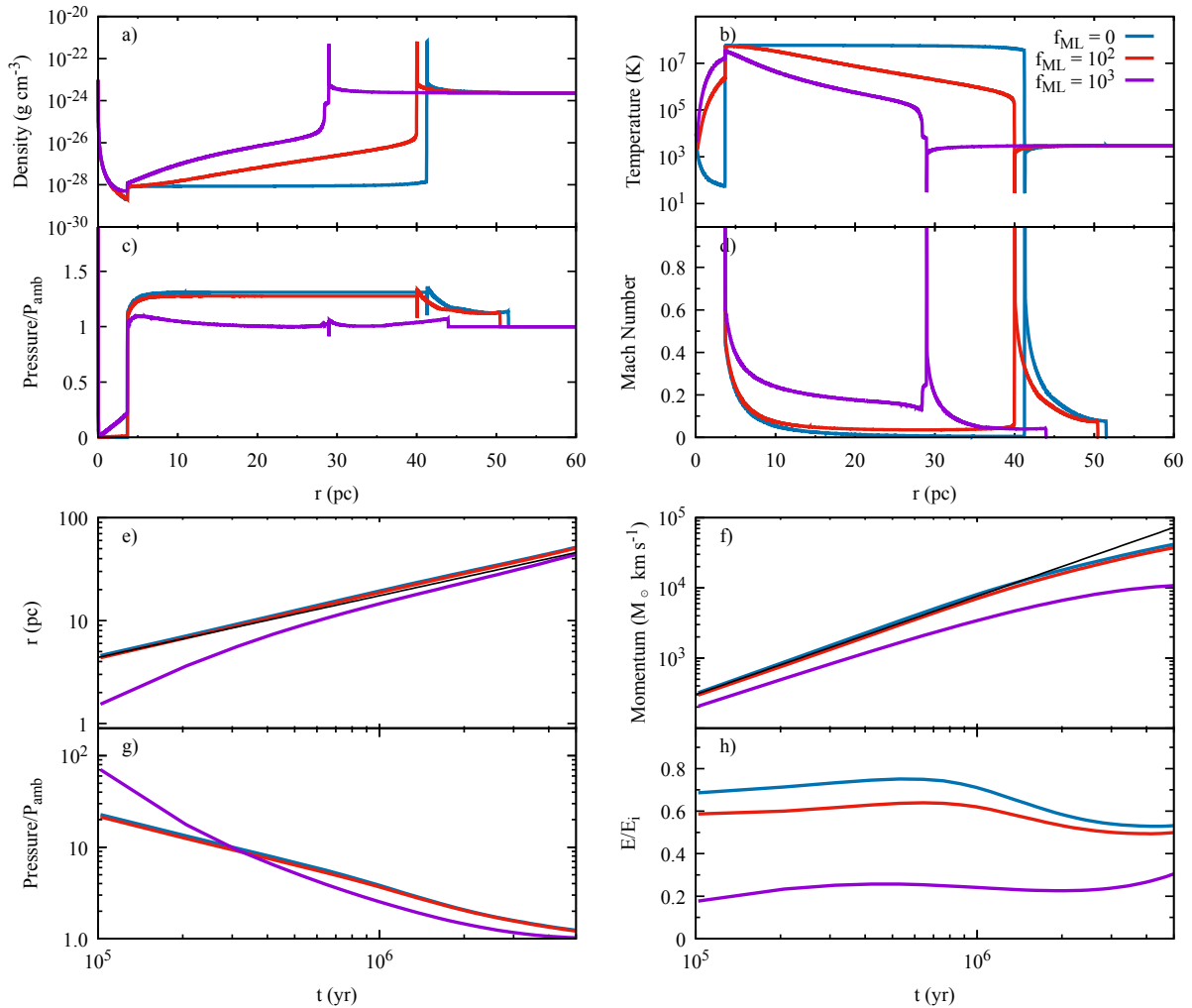


Figure 2. The evolution of a bubble with $n_{H,ic} = 1 \text{ cm}^{-3}$ ($\rho_{ic} = 2.267 \times 10^{-24} \text{ g cm}^{-3}$) and with varying amounts of mass-loading. Strong mass-loading (high values of f_{ML}) results in dramatic changes in the bubble properties. The profiles in panels a-d) are at $t = 5$ Myr.

bubbles must have sufficient resolution such that the reverse shock initially moves away from the edge of the wind injection region, otherwise the amount of PdV work done by the bubble will be underestimated. We have ensured that we have enough resolution in our calculations without mass-loading to meet this requirement, but it is clear that it is not fully met in our $f_{ML} = 10^3$ simulations. However, we can confirm that in higher resolution calculations, a weak reverse shock is established between 2000 – 3000 yr. Although there are some quantitative differences in the profiles and bubble properties at $t = 10^5$ yr, these differences reduce with time (e.g. the difference in the radial momentum at $t > 0.5$ Myr is less than 5 per cent). Likewise, investigation of the $f_{ML} = 10^2$ simulations reveals that the reverse shock is established in the standard resolution calculations by $t = 3100$ yr. Thus we are confident that all of our models are capturing the physics correctly and are accurate enough for our purposes.

So why does the $f_{ML} = 10^3$ bubble evolve so differently to bubbles with $f_{ML} = 0$ and 10^2 ? It is clear that the more highly mass-loaded bubble radiates significantly more energy, with the retained energy fraction falling to about 2 per cent at $t = 10^4$ yr. Thus it appears that the added mass in the bubble causes the bubble to cross a threshold where cooling is finally able to become significant in the bubble

interior⁷. This changes the interior pressure (though not in a simple way due to the frictional effect of the mass-loading), and slows the bubble expansion. Velocities in the bubble are also reduced due to the necessity for the flow and injected mass to conserve momentum.

As the $f_{ML} = 10^3$ bubble expands, the density of the hot interior decreases, and the cooling becomes somewhat less effective, causing the retained energy fraction to increase to a value of about 0.25 for most of the bubble lifetime. Analysis of the cooling in this model indicates that roughly 25 per cent is by gas with $T > 10^5$ K. Concerning the origin of the gas causing the cooling, 22 per cent is from swept-up ambient material, and 78 per cent is from clump material (as indicated by the value of the passive scalar). The clump material is mostly mixed in with the shocked stellar wind and, although it exists at a wide range of temperatures, predominantly cools at $T < 10^5$ K. Nevertheless, the bubble still performs significant PdV work during its life, boosting the momentum input by the wind by a factor of 10.

In summary, mass-loading reduces the retained energy in the bub-

⁷ The effect of strong cooling when bubbles become too mass-loaded has been studied in the case of super-star cluster winds by Wünsch et al. (2011) and Silich & Tenorio-Tagle (2013).

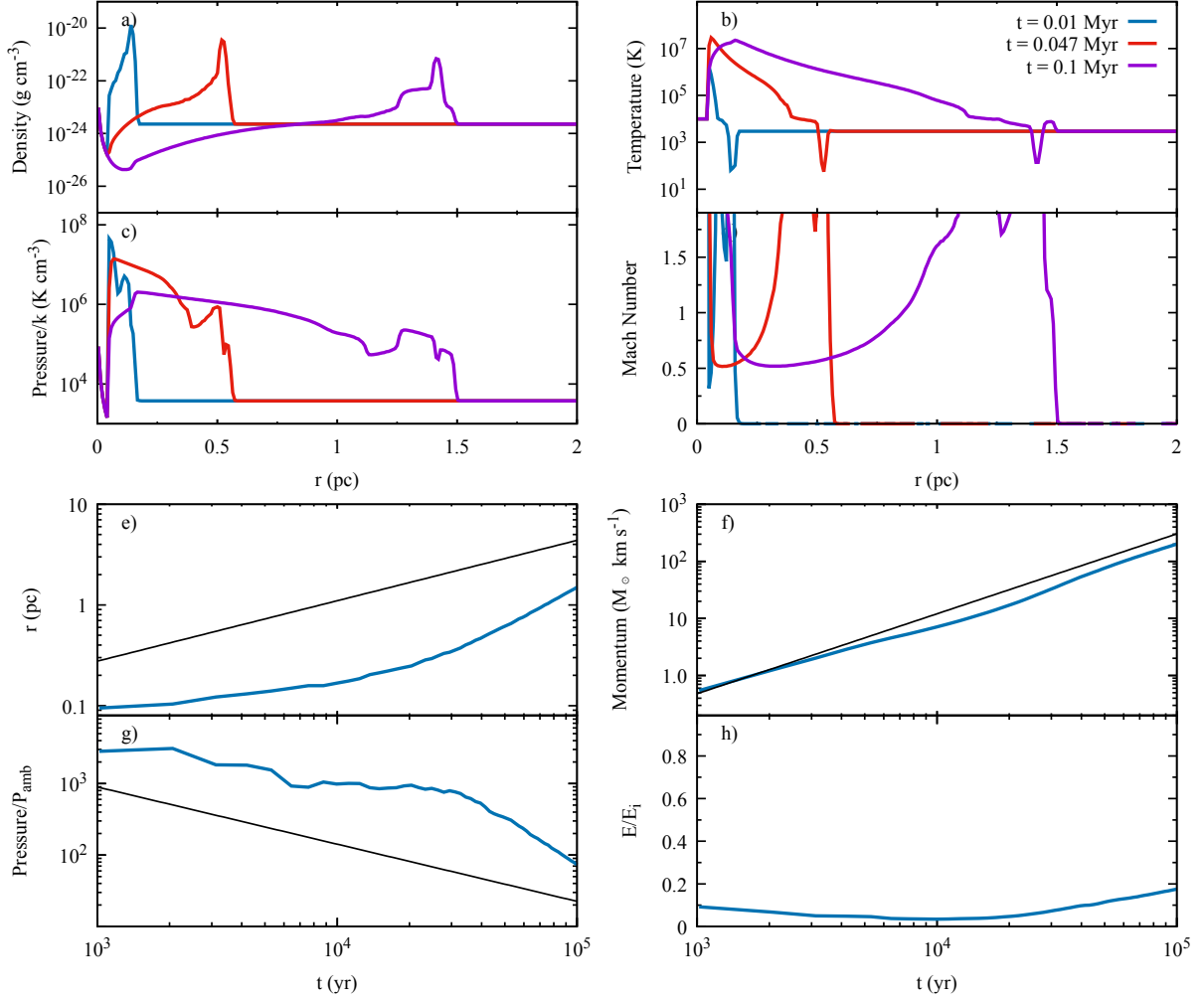


Figure 3. As Fig. 1 but for a bubble with strong mass-loading ($f_{ML} = 10^3$), and with a focus on its early ($t \leq 0.1$ Myr) development.

ble (see Fig. 2h and Table 1), but hot gas is still present in our models which allows the bubble to still do significant PdV work.

3.1.3 A finite amount of clump mass

We now investigate the behaviour of a WBB subject to rapid mass-loading ($f_{ML} = 10^3$) but where there is a finite amount of available mass in the clumps. Fig. 5a-d) shows density, temperature, pressure and Mach number profiles in this case. We see that when there is equal mass in the clumps and intercloud gas (i.e. $\nu = 1$), the WBB still shows the effects of significant mass-loading. This is because the average smeared out density of the clumps, which is equal to the ambient intercloud density, is significantly greater than the density of the shocked wind in the bubble interior, and therefore the injected mass can still dramatically reduce the temperature of the bubble interior.

However, when only 1 per cent of the background mass is in clumps (i.e. $\nu = 0.01$), Fig. 5 shows that there is insufficient mass in the clumps to significantly affect the bubble interior, which now resembles that of a bubble without any mass-loading. Fig. 6 shows the clump survival fraction for these simulations, which we define as the fraction of the initial clump mass that still remains (i.e. the current value of $\rho_{cl,avg}$ divided by its initial value). When $\nu = 0.01$,

we see that clumps are only present in the region of swept-up gas, and that interior to the contact discontinuity no clumps survive. Thus the ongoing mass-loading actually occurs only in the swept-up shell. Clumps that are overrun by the bubble do not survive their passage through the thick shell, and none reach the low density, hot interior gas.

Most interestingly, we see that the $\nu = 0.1$ simulation represents an intermediate stage where the clumps have enough total mass to significantly affect the density, temperature, pressure and Mach number of the bubble interior, but not enough mass to ensure that mass-loading continues in all parts of the bubble over its entire life. In this case, at $t = 5$ Myr, no clumps survive at $r < 19$ pc. This arises from the fact that the clouds that are closest to the central star interact with the bubble at earlier times than more distant clouds, and the mass injected from the clouds is swept downstream towards the edge of the bubble⁸. This has an interesting effect on the $\nu = 0.1$ profiles shown in Fig. 5. We see a significant density enhancement only for $r > 19$ pc, where the temperature rapidly drops and the Mach number climbs as mass-loading continues from the parts of the mass reservoir that are as yet undepleted. However, between the reverse

⁸ In reality the clouds will likely pick up some momentum while they are being destroyed.

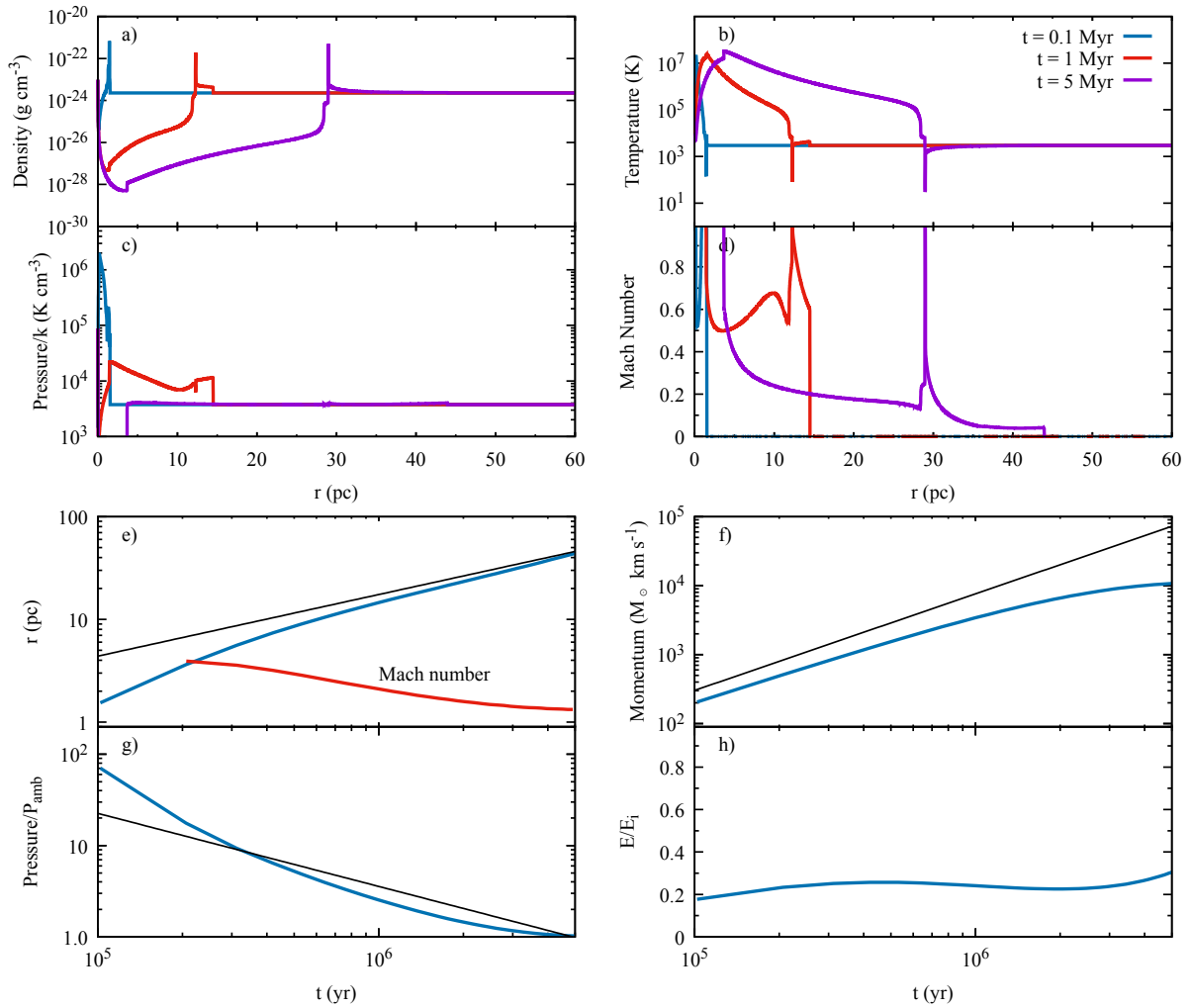


Figure 4. As Fig. 3 but focusing on the later ($t \geq 0.1$ Myr) development of the bubble.

shock at $r = 4.3$ pc and $r = 19$ pc, the temperature of the gas is $\approx 5 \times 10^7$ K (essentially that of a bubble without any mass-loading).

In Fig. 5e)-h) we show the radius, radial momentum, pressure and retained energy of the bubble as a function of time. We see that the radius of the forward shock in the model with $\nu = 0.1$ at first diverges from the $\nu = 0.01$ case, but after 2 – 3 Myr it begins to converge again as the relative lack of clump mass begins to be felt. Fig. 5f) reveals that when $\nu = 0.1$ the radial momentum plateaus at late times. Clearly the mass-loading at early times for the $\nu = 0.1$ case is somewhat constrained by the available reservoir of cloud mass (note that the momentum is initially much closer to the $\nu = 0.01$ case than the $\nu = 1$ case), but by $t = 1$ Myr a significant momentum difference has arisen between the $\nu = 0.01$ and $\nu = 0.1$ simulations. This difference increases with time until the end of the simulations, so that a significant reduction in the final momentum still occurs when $\nu = 0.1$.

Fig. 5g) shows that the bubble pressure responds in a non-linear way to changes in ν . Within the range $\nu = 0.01 - 1$, increasing ν leads to a reduced bubble pressure at all times. However, when there is an infinite amount of clump mass, the bubble pressure may be greater or smaller than a bubble without mass loading, depending on the bubble age. On the other hand, Fig. 5h) shows that the retained

energy fraction varies in a more straightforward way - the less mass-loading, the higher the retained energy.

3.2 “High” intercloud density

We have also investigated the evolution of WBBs in a denser environment. Specifically we set $n_{\text{H,ic}} = 884 \text{ cm}^{-3}$ ($\rho_{\text{ic}} = 2.0 \times 10^{-21} \text{ g cm}^{-3}$), which gives $T_{\text{ic}} = 21.2$ K. The pressure of the intercloud gas, $P_{\text{ic}} = 1.48 \times 10^{-12} \text{ dyn cm}^{-2}$ ($P_{\text{ic}}/k = 1.075 \times 10^4 \text{ K cm}^{-3}$). With these parameters $r_{\text{inj,max}} = 2.68$ pc. The width of each grid cell is set to $dr = 5.36 \times 10^{-3}$ pc. Fig. 7 and Table 2 show the results for this scenario.

The main difference to the lower density simulations is that the bubble is much smaller at any given time. This results in much higher pressures inside the bubble, and although the ambient pressure is nearly 3 times greater, higher relative pressures in the bubble mean that the ambient pressure remains negligible throughout the simulation: hence the simulation without mass-loading agrees well with simple analytical theory even in the latter stages of the bubble’s evolution.

Examining first the $f_{\text{ML}} = 0$ bubble without any mass-loading, we note that the isothermal Mach number of the forward shock remains high throughout the simulation (at $t = 5$ Myr it has a value of 5.1),

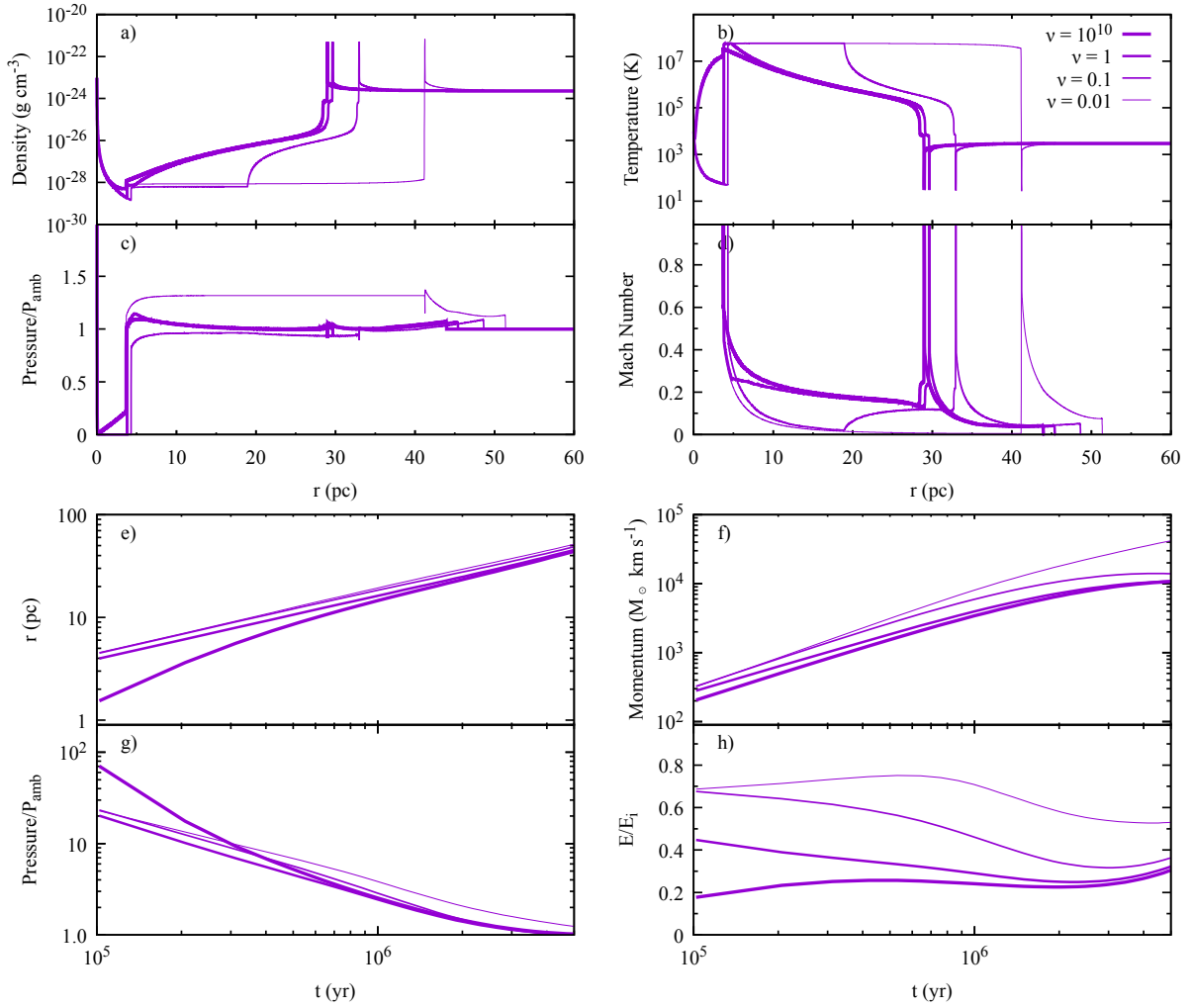


Figure 5. Results from a model with $n_{\text{H,ic}} = 1 \text{ cm}^{-3}$ ($\rho_{\text{ic}} = 2.267 \times 10^{-24} \text{ g cm}^{-3}$), $f_{\text{ML}} = 10^3$ and $\nu = 10^{10}$, 1.0, 0.1 and 0.01. As ν decreases the amount of mass available in the clumps that can be injected into the bubble reduces. The profiles in panels a)-d) are at $t = 5$ Myr.

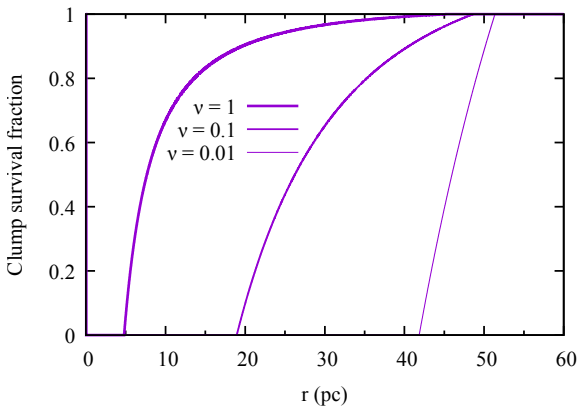


Figure 6. Profiles of the clump survival fraction at $t = 5$ Myr from simulations with $n_{\text{H,ic}} = 1 \text{ cm}^{-3}$ ($\rho_{\text{ic}} = 2.267 \times 10^{-24} \text{ g cm}^{-3}$), $f_{\text{ML}} = 10^3$ and $\nu = 1.0, 0.1$ and 0.01 . As ν decreases the region over which all clumps have been destroyed expands to larger radii.

which causes the swept-up shell to remain thin - the compression at the shell is about a factor of 45. This compression is greater

than the factor of 26 expected from the isothermal Mach number, and the difference arises because the gas doesn't remain isothermal. Instead, the gas temperature decreases from the intercloud ambient temperature of 21.2 K to 11.7 K.

The smaller bubble size leads to significantly higher densities in the shocked stellar wind. The smaller bubble size means that the thermal energy of the swept-up ambient medium ($E_{\text{sw}} = 6.9 \times 10^{47}$ erg) does not add significantly to the total energy of the bubble. Without any mass-loading, we find that the bubble has radiated about 55 per cent of its energy at $t = 0.1$ Myr (significantly more at this stage than the bubble expanding into the lower density environment). The retained energy fraction increases with time as the bubble expands and the density of the shocked wind drops. At $t = 5$ Myr, 42 per cent of the input energy has been radiated away (19 per cent by the swept up gas, and 23 per cent by the shocked wind). Nevertheless, the bubble interior is hot and the bubble is actually able to do more PdV work than the equivalent bubble expanding into a lower density medium, with the momentum boost reaching a factor of 250.

We also see that mass-loading seems to have more of an effect on the bubble radius and momentum for a given value of f_{ML} . There is now a significant difference between the $f_{\text{ML}} = 0$ and $f_{\text{ML}} = 10^2$ models, whereas the differences were minimal when $n_{\text{H,ic}} = 1 \text{ cm}^{-3}$ (see Fig. 2). This seems to be because of the stronger cooling in

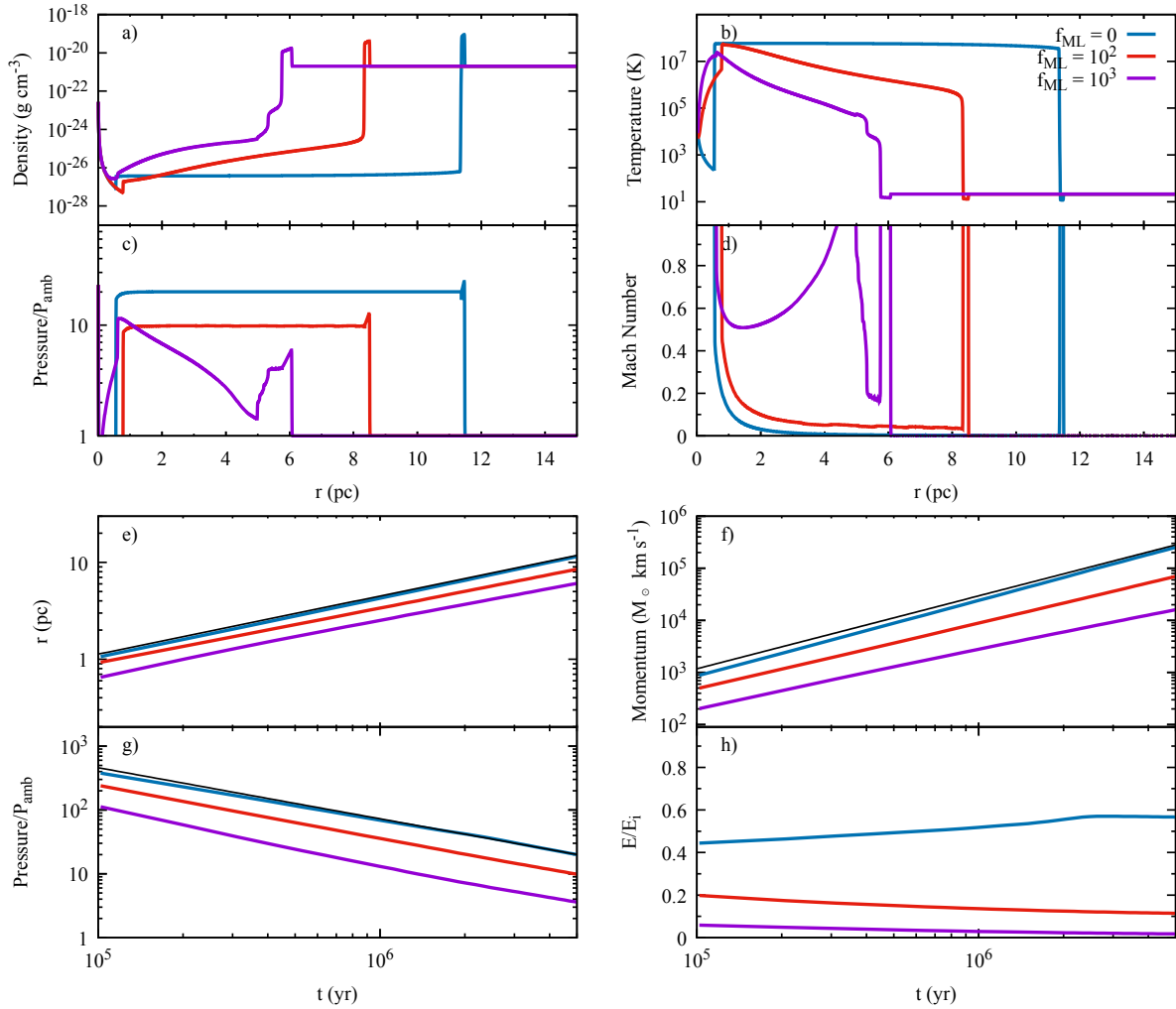


Figure 7. As Fig. 2 but for an intercloud density $n_{\text{H,ic}} = 884 \text{ cm}^{-3}$ ($\rho_{\text{ic}} = 2 \times 10^{-21} \text{ g cm}^{-3}$). The profiles in panels a-d) are at $t = 5 \text{ Myr}$.

the shocked stellar wind, which causes the retained energy fraction to drop to 12 and 2 per cent for $f_{\text{ML}} = 10^2$ and 10^3 , respectively. Thus the threshold mass-loading factor where significant additional radiative cooling occurs is somewhat lower when the intercloud ambient density is higher and the bubble relatively smaller and denser. It is also interesting to see that the retained energy fraction increases or is constant with time for the bubble without mass-loading, but decreases with time for the mass-loaded bubbles.

The final radial momentum in the $f_{\text{ML}} = 10^3$ simulation now decreases to 6 per cent of the value obtained from the equivalent bubble without any mass-loading, though this still represents a factor of 16 boost over the input wind momentum.

4 DISCUSSION

4.1 Validity of the assumptions

A key assumption in this work is that the clouds mix rapidly with the background flow, with negligible radiative losses during this time. The interaction of the hot intercloud gas with the cooler cloud material creates a turbulent mixing layer with a characteristic temperature $T_m = \sqrt{T_h T_c}$, where T_h and T_c are the temperatures of the hot and cold gas, respectively (Begelman & Fabian 1990). The characteristic

number density of the mixing layer $n_m = n_h \sqrt{T_h/T_c} = n_c \sqrt{T_c/T_h}$, where n_h and n_c are the number densities of the hot and cold gas, respectively. An excellent review of the nature of such interfaces is given by Hartquist & Dyson (1988).

Recent numerical studies by Gronke & Oh (2018) showed that clouds in a hot wind are destroyed if

$$t_{\text{cc}} < t_{\text{cool,mix}}, \quad (7)$$

where t_{cc} is the cloud crushing time, and $t_{\text{cool,mix}}$ is the cooling timescale of the mixed gas. Eq. 7 sets an upper limit to the size of the clouds, since $t_{\text{cc}} \propto r_c$, where r_c is the cloud size or radius⁹.

The cooling time of the mixed gas,

$$t_{\text{cool,mix}} = \frac{E}{\dot{E}} = \frac{3 n_m k T_m}{2 n_m^2 \Lambda(T_m)}. \quad (8)$$

Given that $t_{\text{cc}} = \chi^{1/2} r_c / v_{\text{rel}}$, where v_{rel} is the relative velocity between the hot and cold gas, for the cloud to be shredded ($t_{\text{cc}} < t_{\text{cool,mix}}$), we require that

$$r_c < 1.5 \frac{v_{\text{rel}} k T_m}{\sqrt{\chi} n_m \Lambda(T_m)}. \quad (9)$$

⁹ If the opposite is true ($t_{\text{cool,mix}} < t_{\text{cc}}$), hot gas can condense onto the cloud and the cloud can gain mass (Gronke & Oh 2018, 2020).

The value of r_c from Eq. 9 is highly dependent on the temperature of the mixed gas since $\Lambda(T)$ rises so steeply around 10^4 K.

Let us assume that the clouds have a temperature of about 10 K and the hot gas in the bubble is at a temperature of about 10^7 K. This gives a temperature for the mixing layer of about 10^4 K. With our cooling curve, $\Lambda(T) = 10^{-24}$ erg cm³ s⁻¹ when $T = 8700$ K. We will therefore use this value in the following calculations, but note that $\Lambda(T)$ is two orders of magnitude lower at $T = 1600$ K and two orders of magnitude higher at $T = 15,500$ K. The maximum cloud radius that satisfies Eq. 7 will therefore be much smaller (larger) than our estimate if T_m is only slightly higher (lower) than $T = 8700$ K.

We continue by noting that the WBB has a typical overpressure relative to the ambient medium of $10 - 100\times$ (see, e.g., Figs. 1c, 2c and 7c). Taking $P_{\text{amb}}/k \sim 10^4$ K cm⁻³, this means that the embedded clouds have a pressure $P_c/k \sim 10^{5-6}$ K cm⁻³. If $T_c = 10$ K, then $n_c \sim 10^4 - 10^5$ cm⁻³. In the following calculations we assume that $n_c = 10^4$ cm⁻³. With $T_h \approx 10^7$ K, we obtain $\chi = T_h/T_c = n_c/n_h = 10^6$ and $n_h = 10^{-2}$ cm⁻³. This gives $T_m \approx 10^4$ K (we use 8700 K in our calculations) and $n_m = 10$ cm⁻³.

If $v_{\text{rel}} = v_w/4 = 500$ km s⁻¹ (this is typical of the flow speed just after the reverse shock, but the gas slows as it moves towards the contact discontinuity) we obtain $t_{\text{cool,mix}} = 5700$ yr and $r_c < 3 \times 10^{-3}$ pc. Clouds of this size and smaller, with similar densities, have been observed in many H II regions (e.g. de Marco et al. 2006; Gahm et al. 2013; Grenman & Gahm 2014; Haikala et al. 2017). The maximum mass of the cloud is $m_c = 0.03 M_J$ (Jupiter masses). Smaller values of v_{rel} mean longer values of t_{cc} which requires smaller clouds to satisfy Eq. 7. The cooling time of the gas in the mixing layer is similar to the cooling times seen in Figs. 2 and 3 of Lancaster et al. (2021b).

In the $f_{\text{ML}} = 10^3$ simulations with $n_{\text{ic}} = 1$ cm⁻³, $500 M_\odot$ of cloud material was injected into the bubble by $t = 5$ Myr. This corresponds to the destruction of more than 1.8×10^7 clumps, and since the WBB has a radius of 44 pc, the clumps have a volume filling factor of $\sim 10^{-5}$ and thus take up a negligible amount of space within the bubble. The ratio of the total surface area of the clumps to the surface area of the WBB is ≥ 0.1 .

Directly modelling such a range of length scales is impossible with current computational resources. Ideally one would like to have a resolution, Δx , such that there are of order 100 grid cells per cloud radius. This requires that $\Delta x \lesssim 3 \times 10^{-5}$ pc. Capturing the global WBB at the same time as resolving the interaction around individual clouds requires $\geq 10^6$ cells per grid axis, or $\geq 10^{18}$ 3D grid cells. Relaxing the resolution requirements to 10 cells per cloud radius, as suggested by Banda-Barragán et al. (2020), and modelling just one octant requires $\geq 10^{14}$ cells. Due to the turbulent nature of the flow, it is unlikely that adaptive mesh refinement will be of much use. Therefore, our approach of treating the clumps as a continuous distribution is the only feasible method for simulating WBBs that are mass-loaded by small clouds at the current time.

Finally, we note that due to a lack of significant bulk motions in IFU observations of a gas pillar in the H II region NGC 6357, Westmoquette et al. (2010) conjectured that the evaporated and/or ablated gas from the pillar is rapidly heated before it is mixed and/or entrained into the surrounding flow. This provides some observational support for our assumption that the mass injected from clumps into our bubbles does not undergo significant radiative cooling during this process.

We can also wonder what effect the ionizing photons from the cen-

tral star may have on the clumps¹⁰. A star with similar wind properties has a hydrogen ionizing photon flux $Q_H \approx 10^{48}$ s⁻¹ (Sternberg, Hoffmann & Pauldrach 2003). Using the equations in Bertoldi (1989), we find that clouds with $r_c = 3 \times 10^{-3}$ pc and $n_c = 10^4$ cm⁻³ will be instantly ionized (or “zapped”) if closer than 0.13 pc. At a distance of 5 pc from the star, we find that the clouds lie in region II of Fig. 1 in Bertoldi (1989) and so will be compressed by an ionization shock front which is thin compared to the size of the cloud. The ionized gas flows away from the cloud, causing the cloud to lose mass at a rate $\dot{M}_{c,\text{ph}} = mFA$, where m is the mass per particle of the neutral material, and F and A are the rate per unit time per unit area at which hydrogen ionizing photons reach the ionization front and its area, respectively (Mellema et al. 1998). To first order, the lifetime of the clump before it is completely photoevaporated is $t_{\text{life,ph}} = M_c/\dot{M}_{c,\text{ph}}$ (this is a lower limit since in reality the mass-loss rate decreases with time). We estimate that $F = F_0/1.1$, where $F_0 = Q_H/4\pi d^2$, giving $\dot{M}_{c,\text{ph}} = 1.3 \times 10^{17}$ g s⁻¹. The cloud will then have a lifetime of approximately 1.3×10^4 yr. Much smaller clouds will lie in region V, whereby the ionization-front-driven shock sweeps rapidly over the cloud. Clouds which are further from the star will have lower rates of photoevaporation (smaller $\dot{M}_{c,\text{ph}}$) and longer lifetimes. Since the cloud crushing time, $t_{\text{cc}} = 5700$ yr, $t_{\text{life,ph}}$ and the cloud mixing time, t_{mix} , are of similar magnitude¹¹. Hence, in reality both hydrodynamic ablation and photoevaporation likely play a role in destroying the clouds.

To summarize, the requirement that the cloud mixing time be less than the cooling time of the mixed gas requires that our embedded clouds have radii $r_c \lesssim 3 \times 10^{-3}$ pc. Significantly smaller clouds may be immediately zapped by the ionizing radiation from the central star. Clouds at this size limit will instead have a lifetime against photoevaporation of order 1.3×10^4 yr. Clouds may also lose mass through thermal conduction (see Pittard 2007, for a discussion of these different mechanisms). Our numerical values, are, however, very sensitive to the temperature of the gas in the mixing layer. If this is slightly lower than we have assumed, much larger clouds can be destroyed, and fewer clouds are needed to provide the required mass injection into the bubble. This could easily arise in situations where the temperature of the hot gas is a little lower than we have assumed (e.g. if $v_w < 2000$ km s⁻¹, or if the cloud is interacting with part of the flow that has already experienced some mass-loading). However, if T_m is only slightly higher than we have assumed, the hot-phase gas will instead try to condense onto the cold clouds (although in this case the clouds likely still lose mass due to photoevaporation). Irrespective of how the clouds lose mass, the mass injected into the surrounding flow can have a significant effect on the global properties of the flow, as this work shows.

4.2 Comparison to previous mass-loading simulations

Similarity solutions of mass-loaded WBBs were obtained by Pittard, Dyson & Hartquist (2001) and Pittard, Hartquist & Dyson (2001). They found that with extremely high mass-loading the wind could be slowed to such an extent that it connects directly to the contact discontinuity, without the presence of a reverse shock. Although we

¹⁰ In reality, the stellar wind will always interact with a H II region where clumps are subject to the “rocket effect” which homogenizes the region that the wind is interacting with (Elmegreen 1976; McKee, Van Buren & Lazareff 1984).

¹¹ In adiabatic hydrodynamic simulations, $t_{\text{mix}} \approx 5 - 15 t_{\text{cc}}$ (Pittard & Parkin 2016; Pittard & Goldsmith 2016).

find that vigorous mass-loading slows the creation of a reverse shock (see Fig. 3), all of our models have a reverse shock by $t = 0.1$ Myr. A reverse shock still forms when $f_{\text{ML}} = 10^4$, but when $f_{\text{ML}} = 10^5$ the reverse shock completely disappears and is not present at $t = 5$ Myr. We also find that for $f_{\text{ML}} = 10^4$ and 10^5 , the final radial momentum slightly *exceeds* that obtained when $f_{\text{ML}} = 10^3$ (at $t > 3$ Myr; before this time the radial momentum is lower)¹². Such strong mass-loading is unlikely to occur in real WBBs.

To obtain the similarity solutions the mass injection rate from the clumps must be radially dependent. For a stellar wind with a time independent mechanical luminosity and an intercloud ambient medium of constant density, it is required that $\dot{\rho} \propto r^{-5/3}$. As $\dot{\rho}$ is not spatially dependent in our current work (though it does decrease with time), further comparison to these papers is unfortunately not possible.

Arthur et al. (1993, 1996) used hydrodynamical simulations to investigate mass-loading in the RCW 58 WBB. They assumed that the volumetric mass injection rate only depended on the Mach number of the flow, and adopted the prescription of Hartquist et al. (1986). Since the mass loading results in a fairly constant $M \approx 0.6-0.7$ in the bubble interior, it is clear that as the bubble grows, the global mass injection rate increases in their simulations. This again differs from our work, where the global rate of mass injection remains constant (unless the clump mass reservoir runs out). It is unclear which of these different scenarios best represents reality, and in any case the specific clump distribution may vary from object to object. Nevertheless, the same general effects due to the mass-loading are observed.

Arthur (2012) simulated the Orion nebula as a combined WBB and H II region, including mass-loading from the embedded proplyds and from thermal conduction at the edge of the hot bubble. The mass-loading rate due to the proplyds was assumed to be radially dependent, following the observed spatial density distribution of the proplyds. A mixing efficiency of 10 per cent was assumed for the injected mass, but since the post-shock bubble temperature was found to be higher than observed, a higher mixing efficiency might be appropriate. Alternatively, oblique shocks and/or the downstream turbulence generated by many mass-loading sources on a flow may play a role in reducing the post-shock temperature (Pittard et al. 2005; Alūzas et al. 2012).

In comparison to our new work, previous works which modelled mass-loaded bubbles by treating clumps in the continuous limit have two main shortcomings. Firstly, they allow for an infinite reservoir of clump mass, which allows mass-injection to occur at all radii, whereas in reality the bubbles are likely to become devoid of clumps in their central regions as the clumps are destroyed (see, e.g., Fig. 3 in Rogers & Pittard (2013) and Figs. 5 and 6). Secondly, the Mach-number dependent mass-injection rate used in Arthur et al. (1993, 1996) is based on an incorrect scaling (see Pittard et al. 2010).

We also note that the global normalization of the mass injection rate is simply scaled in these earlier models, whereas in reality it is likely to depend in some way on the stellar mass-loss rate or on the

stellar ionizing photon flux (if hydrodynamic ablation or photoevaporation is the dominant mixing process, respectively). For instance, Fig. 10 in Rogers & Pittard (2013) shows that the mass-loading factor of the outflow from a stellar cluster increases when each star enters their Wolf-Rayet phase. Having said this, it is also clear that the scaling is not necessarily a linear one and is also likely to be time dependent.

McKee et al. (1984) hypothesized that stellar wind bubbles are made radiative by mass input from photoevaporating clumps, and for this reason Matzner (2002) assumed that WBBs do not generate momentum in excess of the wind momentum itself. In other words, mass-loading “quenches” the bubble. Recent numerical simulations of WBBs expanding into a turbulent medium show that efficiently cooled bubbles that approach momentum-conserving-like behaviour can exist (Lancaster et al. 2021b). However, examination of Fig. 10 in this work reveals that in 7 out of 12 simulations the fractional turbulence shows a significant drop before the bubble breaks out of the simulation domain, while Fig. 8 shows that the momentum enhancement factor in nearly all cases is rising with time. This perhaps opens the door for a later transition to energy-conserving-like behaviour, although in most cases it would likely not arise before the wind bubble has broken out of its local cloud environment when the nature of the bubble becomes drastically different. As noted in the introduction, the cooling at the interface between hot and cold gas in these simulations may also be overestimated.

Lancaster et al. (2021a) find that due to efficient cooling in their WBBs, the bubble pressure is substantially lower than that of the standard Weaver et al. (1977) bubble (see, e.g., their Fig. 2). In this respect our results are quite different, as we find mass-loading with $f_{\text{ML}} = 10^2$ slightly reduces the bubble pressure, but that stronger mass-loading with $f_{\text{ML}} = 10^3$ first increases the bubble pressure over the Weaver et al. (1977) value, and then decreases it (see panel g in Figs. 2-4). Fig. 17 in Lancaster et al. (2021b) shows that the retained energy fraction in their simulations is typically ~ 0.1 at early times, and decreases with time, reaching ~ 0.01 at later times. This level of cooling is stronger than in our low ambient density simulations, where for $f_{\text{ML}} = 10^3$ this fraction is $0.2-0.3$ over most of the bubble life (see Fig. 2h). Ultimately, this difference allows our bubble to do more PdV work and reach a relatively higher radial momentum. However, in our simulations at higher ambient density, strong mass-loading can cause the bubble to radiate 98 per cent of the input energy. This finding is in better agreement with those of Lancaster et al. (2021b), though again we find a significant momentum boost.

Finally, we note that Pittard (2019) investigated mass-loading in simulations of SNRs expanding into an inhomogeneous environment, using the same approach as this work. Since the final radial momentum was usually reduced by less than a factor of two, it appears that WBBs are more sensitive to mass-loading than SNRs. On the other hand, we note that heavily mass-loaded SNRs are not able to regenerate high temperature gas if all the clumps within a specific region are destroyed, unlike the behaviour we find for WBBs (see Fig. 5).

4.3 Comparison to observations

The environment that bubbles expand into is typically clumpy, so they are expected to undergo some form of mass-loading. Bubbles can be blown by single massive stars which are either young or evolved, or by groups of massive stars in stellar clusters. Let us first consider young, single massive stars. One of the most interesting studies to date is of N49, a dusty WBB blown by an O5V star with an age of $0.5-1.0$ Myr (Everett & Churchwell 2010). Because of the inferred short lifetime of the dust, dusty gas is thought to be continuously injected into

¹² The $f_{\text{ML}} = 10^5$ bubble at $t = 5$ Myr has some similarities to the $f_{\text{ML}} = 10^3$ bubble at very early times (see Fig. 3). Only a small amount of gas near the center of the bubble where the stellar wind starts being mass-loaded is hot. This gas rapidly heats due to the frictional heating of the mass-loading, but soon reaches a peak temperature and at greater radii becomes cooler as the continued mass-loading shares out the thermal energy amongst more particles. Almost all of the gas in the bubble is substantially denser than the ambient intercloud gas, and is cold with temperatures of ≈ 20 K. High pressures arise during the initial frictional heating which we believe are ultimately responsible for the slightly higher momentum at late times.

the bubble by high density clouds ($n \sim 10^5 \text{ cm}^{-3}$) that are overrun and engulfed. The mass-loss rate of the central star is estimated as $\dot{M}_w = 1.5 \times 10^{-6} M_\odot \text{ yr}^{-1}$, while the clump injection rate is estimated as $\dot{M}_{cl} = 2.5 \times 10^{-4} M_\odot \text{ yr}^{-1}$. This gives a mass-loading strength $f_{ML} = \dot{M}_{cl}/\dot{M}_w \approx 150$. The total mass injected by the clumps so far is thought to be $125 - 250 M_\odot$. The external intercloud density is not well constrained but estimated to have a number density $n_H \sim 10^4 \text{ cm}^{-3}$. Since the radius of the bubble is 2 pc, the swept-up mass is $1.12 \times 10^4 M_\odot$. This gives a minimum value for the clump to interclump mass ratio $\nu = 125/11200 = 0.011$. Comparison with Fig. 7 suggests that the mass-loading in N49 might significantly affect the bubble properties, though whether this is actually the case will depend on whether the available reservoir of clump mass is large enough (cf. Fig. 5).

Everett & Churchwell (2010) also note that if the dust is gradually evaporated there should be bubbles with a central dust-free region, where the $24 \mu\text{m}$ emission from the injected dust is confined to a bright rim. It would be interesting to perform a full radiation hydrodynamics model of the combined H II region and WBB of N49, with mass-loading from dusty embedded clumps, to compare to the available data. However, this is beyond the scope of the current paper.

Indirect evidence for mass-loading in WBBs also comes from the lower than expected X-ray temperatures that have been measured. However, X-ray emission is currently very difficult to detect in WBBs produced by single unevolved stars. No X-ray emission was detected from the iconic Bubble Nebula (NGC 7635), for instance (Toalá et al. 2020). However, X-ray emission has been detected in the Extended Orion Nebula, which is powered mainly by the star $\theta^1 \text{ Ori C}$ (Güdel et al. 2008), and in the WBB around $\zeta \text{ Oph}$ (Toalá et al. 2016a).

X-ray emission is more readily detected in WR nebulae, though only 4 have detected X-ray emission to date: S 308, NGC 2359, NGC 3199, and NGC 6888, around WR 6, WR 7, WR 18 and WR 136, respectively (e.g. Toalá et al. 2012, 2014, 2015, 2016b, 2017). The properties of the emission, including its relative softness, brightness, and the inferred abundances and estimated electron density of the hot gas, favour a scenario in which strong mixing of circumstellar material from the outer shell (formed from the sweeping up of a previous, slower wind) into the bubble interior occurs. This process may be aided by the fragmentation of the shell, which results in dense clumps becoming embedded in the hot interior gas (e.g. Toalá & Arthur 2011). Such a scenario is not radically different from the work presented here: the main difference is that the clumps originate from previous mass-loss from the star rather than from the wider interstellar medium.

Finally, we note that X-ray emission has also been detected in young (pre-SN) massive clusters, such as M17 and the Rosette Nebula (Townsley et al. 2003). It is thought that the X-ray emission arises from the collective thermalization of the stellar winds, and softened by mass-loading from embedded clumps and adjacent colder surfaces (Townsley et al. 2011a). In some objects the nearest embedded clumps may have been destroyed/cleared away, with ongoing mass-loading of the flow occurring only at greater distances. Such faint diffuse X-ray emission seems to be a ubiquitous property of massive star forming regions (e.g. Townsley et al. 2011b, 2014, 2018, 2019). Dedicated modelling of specific clusters is needed to make further progress, such as has been attempted for M17 (Reyes-Iturbide et al. 2009; Velázquez et al. 2013) and the Rosette Nebula (Wareing et al. 2018).

5 SUMMARY AND CONCLUSIONS

We have examined the properties and behaviour of wind-blown bubbles expanding into a clumpy, inhomogeneous medium. The expanding bubble is assumed to sweep up intercloud material, and to sweep over pre-existing clouds which are destroyed within it as they become overrun/engulfed. The cloud destruction adds mass into the bubble, which we assume rapidly merges with the global flow and attains the same density, velocity and temperature. We assume that the mixing timescale of the gas is much shorter than the cooling timescale of the mixing gas, so that there is no significant cooling during this transition. The nature of the mass-loading is parameterized by two variables: the mass-loading strength, $f_{ML} = \dot{M}_{cl}/\dot{M}_w$, and the ratio of cloud to intercloud mass per unit volume in the ambient medium, ν . The mass injection is assumed to occur uniformly within the bubble, unless and until the available mass reservoir at a particular radius is exhausted.

We find that:

(i) Mass injection can affect the behaviour and evolution of the bubble from its earliest stages. It increases the density and decreases the velocity within the bubble. In the pre-shock stellar wind it increases the temperature through drag heating, while it reduces the temperature of hot shocked gas as the available energy is shared between more particles. The affect of mass-loading on the volume-averaged pressure in the bubble is more complicated, and may increase or decrease it (in some cases this depends also on the bubble age). However, mass-loading always enhances the radiative cooling and reduces the retained energy fraction.

(ii) Mass-loaded bubbles do not expand as quickly or as far. They cool more quickly, do less PdV work on the swept-up gas, and ultimately attain a lower final momentum. However, they can still provide a significant boost to the radial momentum input by the wind. This is especially true if the mass-loading is relatively weak and/or the available mass in clouds is relatively low. However, even when cooling losses become severe, and the retained energy fraction drops to very low values, we find that the bubble may still substantially boost the wind momentum. In this respect, our mass-loaded bubbles behave more like energy-conserving bubbles, rather than the momentum-conserving-like behaviour of “quenched” bubbles.

(iii) If the available clump mass is limited and starts to run out, the reduction to the final radial momentum is not as severe. In some cases, parts of the bubble may become clump free and not subject to any current mass-loading, while other parts may still contain clumps and continue to be mass-loaded. This can create interesting density and temperature profiles. In such cases, high temperature gas can be regenerated (unlike in SNRs).

(iv) Mass-loading also drag heats the stellar wind prior to its thermalization at the reverse shock. In extreme cases the reverse shock no longer exists, though this is unlikely to occur in real bubbles.

In summary, mass-loading can significantly affect the behaviour of WBBs. However, we find that for the model parameters explored in this work, the bubbles can still perform significant PdV work on the surrounding gas, and provide substantial boosts to the radial momentum input by the wind.

ACKNOWLEDGEMENTS

We thank Joshua Selby for running some simulations in the very early stages of this work, and the referee for very detailed and useful suggestions. We acknowledge support from the Science and Technology Facilities Council (STFC, Research Grant ST/P00041X/1).

DATA AVAILABILITY

The data underlying this article are available in the Research Data Leeds Repository, at <https://doi.org/10.5518/1183>.

REFERENCES

- Alúzar R., Pittard J. M., Hartquist T. W., Falle S. A. E. G., Langton R., 2012, *MNRAS*, 425, 2212
- Alúzar R., Pittard J. M., Falle S. A. E. G., Hartquist T. W., 2014, *MNRAS*, 444, 971
- Arthur S. J., 2012, *MNRAS*, 421, 1283
- Arthur S. J., Dyson J. E., Hartquist T. W., 1993, *MNRAS*, 261, 425
- Arthur S. J., Dyson J. E., Hartquist T. W., 1994, *MNRAS*, 269, 1117
- Arthur S. J., Henney W. J., Dyson J. E., 1996, *A&A*, 313, 897
- Banda-Barragán W. E., Brügger M., Federrath C., Wagner A. Y., Scannapieco E., Cottle J., 2020, *MNRAS*, 499, 2173
- Banda-Barragán W. E., Brügger M., Heesen V., Scannapieco E., Cottle J., Federrath C., Wagner A. Y., 2021, *MNRAS*, 506, 5658
- Banda-Barragán W. E., Zertuche F. J., Federrath C., García Del Valle J., Brügger M., Wagner A. Y., 2019, *MNRAS*, 486, 4526
- Begelman M. C., Fabian A. C., 1990, *MNRAS*, 244, 26
- Bertoldi F., 1989, *ApJ*, 346, 735
- Brügger M., Scannapieco E., 2016, *ApJ*, 822, 31
- Chevance M., et al., 2022, *MNRAS*, 509, 272
- Colella P., Woodward P. R., 1984, *J. Comp. Phys.*, 54, 174
- Cowie L.L., McKee C.F., 1977, *ApJ*, 211, 135
- Cowie L.L., McKee C.F., Ostriker J.P., 1981, 247, 908
- de Marco O., O'Dell C. R., Gelfond P., Rubin R. H., Glover S. C. O., 2006, *AJ*, 131, 2580
- Dyson J. E., Williams D. A., 1980, *The Physics of the Interstellar Medium*. Halsted Press, New York
- El-Badry K., Ostriker E. C., Kim C.-G., Quataert E., Weisz D. R., 2019, *MNRAS*, 490, 1961
- Elmegreen B. G., 1976, *ApJ*, 205, 405
- Everett J. E., Churchwell E., 2010, *ApJ*, 713, 592
- Farber R. J., Gronke M., 2022, *MNRAS*, 510, 551
- Fielding D. B., Bryan G. L., 2022, *ApJ*, 924, 82
- Fielding D. B., Ostriker E. C., Bryan G. L., Jermyn A. S., 2020, *ApJL*, 894, L24
- Forbes J. C., Lin D. N. C., 2019, *AJ*, 158, 124
- Gahm G. F., Persson C. M., Mäkelä M. M., Haikala L. K., 2013, *A&A*, 555, A57
- García-Segura G., Franco J., 1996, *ApJ*, 469, 171
- Goldsmith K. J. A., Pittard J. M., 2016, *MNRAS*, 461, 578
- Goldsmith K. J. A., Pittard J. M., 2017, *MNRAS*, 470, 2427
- Goldsmith K. J. A., Pittard J. M., 2018, *MNRAS*, 476, 2209
- Goldsmith K. J. A., Pittard J. M., 2020, *MNRAS*, 491, 4783
- Grenman T., Gahm G. F., 2014, *A&A*, 565, A107
- Grevesse N., Asplund M., Sauval A. J., Scott P., 2010, *Ap&SS*, 328, 179
- Gronke M., Oh S. P., 2018, *MNRAS*, 480, L111
- Gronke M., Oh S. P., 2020, *MNRAS*, 492, 1970
- Güdel M., Briggs K. R., Montmerle T., Audard M., Rebull L., Skinner S. L., 2008, *Science*, 319, 309
- Haikala L. K., Gahm G. F., Grenman T., Mäkelä M. M., Persson C. M., 2017, *A&A*, 602, A61
- Hartquist T. W., Dyson J. E., 1988, *Ap&SS*, 144, 615
- Hartquist T. W., Dyson J. E., Pettini M., Smith L. J., 1986, *MNRAS*, 221, 715
- Katz N., 1992, *ApJ*, 391, 502
- Kim C.-G., Ostriker E. C., Raileanu R., 2017, *ApJ*, 834, 25
- Klein R. I., McKee C. F., Colella P., 1994, *ApJ*, 420, 213
- Koo B.-C., McKee C. F., 1992, *ApJ*, 388, 93
- Korolev V.V., Vasiliev E.O., Kovalenko I.G., Shchekinov Y.A., 2015, *ARep*, 59, 690
- Kupilas M. M., Wareing C. J., Pittard J. M., Falle S. A. E. G., 2021, *MNRAS*, 501, 3137
- Lancaster L., Ostriker E. C., Kim J.-G., Kim C.-G., 2021a, *ApJ*, 914, 89
- Lancaster L., Ostriker E. C., Kim J.-G., Kim C.-G., 2021b, *ApJ*, 914, 90
- Marcolino W. L. F., Bouret J.-C., Rocha-Pinto H. J., Bernini-Peron M., Vink J. S., 2022, *MNRAS*, 511, 5104
- Matzner C. D., 2002, *ApJ*, 566, 302
- McCourt M., O'Leary R. M., Madigan A.-M., Quataert E., 2015, *MNRAS*, 449, 2
- McKee C. F., Van Buren D., Lazareff B., 1984, *ApJL*, 278, L115
- Meaburn J., Nicholson R., Bryce M., Dyson J. E., Walsh J. R., 1991, *MNRAS*, 252, 535
- Mellema G., Raga A. C., Cantó J., Lundqvist P., Balick B., Steffen W., Noriega-Crespo A., 1998, *A&A*, 331, 335
- Nakamura F., McKee C. F., Klein R. I., Fisher R. T., 2006, *ApJSS*, 164, 477
- Parkin E. R., Pittard J. M., 2010, *MNRAS*, 406, 2373
- Pittard J. M., 2007, in Harquist T. W., Pittard J. M., Falle S. A. E. G., eds, *Diffuse Matter from Star Forming Regions to Active Galaxies - A Volume Honouring John Dyson, Astrophysics and Space Science Proceedings*. Springer, Dordrecht, p. 245
- Pittard J. M., 2019, *MNRAS*, 488, 3376
- Pittard J. M., Dyson J. E., Falle S. A. E. G., Hartquist T. W., 2005, *MNRAS*, 361, 1077
- Pittard J. M., Dyson J. E., Hartquist T. W., 2001, *A&A*, 367, 1000
- Pittard J. M., Goldsmith K. J. A., 2016, *MNRAS*, 458, 1139
- Pittard J. M., Hartquist T. W., Dyson J. E., 2001, *A&A*, 373, 1043
- Pittard J. M., Hartquist T. W., Falle S. A. E. G., 2010, *MNRAS*, 405, 821
- Pittard J. M., Kupilas M. M., Wareing C. J., 2022, *MNRAS*, 510, 2797
- Pittard J. M., Parkin E. R., 2016, *MNRAS*, 457, 4470
- Pittard J. M., Wareing C. J., Kupilas M. M., 2021, *MNRAS*, 508, 1768
- Poludnenko A. Y., Frank A., Blackman E. G., 2002, *ApJ*, 576, 832
- Reyes-Iturbide J., Velázquez P. F., Rosado M., Rodríguez-González A., González R. F., Esquivel A., 2009, *MNRAS*, 394, 1009
- Rogers H., Pittard J. M., 2013, *MNRAS*, 431, 1337
- Scannapieco E., Brügger M., 2015, *ApJ*, 805, 158
- Schneider E. E., Robertson B. E., 2017, *ApJ*, 834, 144
- Shetty R., Ostriker E. C., 2012, *ApJ*, 754, 2
- Silich S., Tenorio-Tagle G., 2013, *ApJ*, 765, 43
- Slavin J.D., Smith R.K., Foster A., Winter H.D., Raymond J.C., Slane P.O., Yamaguchi H., 2017, *ApJ*, 846, 77
- Smith L. J., Pettini M., Dyson J. E., Hartquist T. W., 1984, *MNRAS*, 211, 679
- Sternberg A., Hoffmann T. L., Pauldrach A. W. A., 2003, *ApJ*, 599, 1333
- Sutherland R. S., 2010, *Ap&SS*, 327, 173
- Toalá J. A., Arthur S. J., 2011, *ApJ*, 737, 100
- Toalá J. A., Guerrero M. A., Chu Y.-H., Arthur S. J., Tafuya D., Gruendl R. A., 2016b, *MNRAS*, 456, 4305
- Toalá J. A., Guerrero M. A., Chu Y.-H., Gruendl R. A., 2015, *MNRAS*, 446, 1083
- Toalá J. A., Guerrero M. A., Chu Y.-H., Gruendl R. A., Arthur S. J., Smith R. C., Snowden S. L., 2012, *ApJ*, 755, 77
- Toalá J. A., Guerrero M. A., Gruendl R. A., Chu Y.-H., 2014, *AJ*, 147, 30
- Toalá J. A., Guerrero M. A., Todt H., Sabin L., Oskinova L. M., Chu Y.-H., Ramos-Larios G., Gómez-González V. M. A., 2020, *MNRAS*, 495, 3041
- Toalá J. A., Marston A. P., Guerrero M. A., Chu Y.-H., Gruendl R. A., 2017, *ApJ*, 846, 76
- Toalá J. A., Oskinova L. M., González-Galán A., Guerrero M. A., Ignace R., Pohl M., 2016a, *ApJ*, 821, 79
- Townsley L. K., Broos P. S., Chu Y.-H., Gruendl R. A., Oey M. S., Pittard J. M., 2011a, *ApJSS*, 194, 16
- Townsley L. K., Broos P. S., Garmire G. P., Anderson G. E., Feigelson E. D., Naylor T., Povich M. S., 2018, *ApJSS*, 235, 43
- Townsley L. K., Broos P. S., Garmire G. P., Bouwman J., Povich M. S., Feigelson E. D., Getman K. V., Kuhn M. A., 2014, *ApJSS*, 213, 1
- Townsley L. K., Broos P. S., Garmire G. P., Povich M. S., 2019, *ApJSS*, 244, 28
- Townsley L. K., et al., 2011b, *ApJS*, 194, 15
- Townsley L. K., Feigelson E. D., Montmerle T., Broos P. S., Chu Y.-H., Garmire G. P., 2003, *ApJ*, 593, 874
- Velázquez P. F., Rodríguez-González A., Esquivel A., Rosado M., Reyes-Iturbide J., 2013, *ApJ*, 767, 69
- Wareing C. J., Pittard J. M., Falle S. A. E. G., 2017a, *MNRAS*, 465, 2757

- Wareing C. J., Pittard J. M., Falle S. A. E. G., 2017b, MNRAS, 470, 2283
Wareing C. J., Pittard J. M., Wright N. J., Falle S. A. E. G., 2018, MNRAS, 475, 3598
Weaver R., McCray R., Castor J., Shapiro P., Moore R., 1977, ApJ, 218, 377
Westmoquette M. S., Slavin J. D., Smith L. J., Gallagher III J. S., 2010, MNRAS, 402, 152
Wünsch R. W., Silich S., Palous J., Tenorio-Tagle G., Muñoz-Tuñón C., 2011, ApJ, 740, 75
Zhang G.-Y., Chevalier R.A., 2019, MNRAS, 482, 1602

This paper has been typeset from a \TeX/L\AA\TeX file prepared by the author.